

## Article

# Influence of Thermo-Mechanical Process and Nb-V Microalloying on Microstructure and Mechanical Properties of Fe–Mn–Al–C Austenitic Steel

Ting Zhao <sup>1</sup>, Xiaohong Hao <sup>1</sup>, Yuefeng Wang <sup>1</sup>, Chen Chen <sup>1,2</sup> and Tiansheng Wang <sup>1,2,\*</sup> 

<sup>1</sup> State Key Laboratory of Metastable Materials Science and Technology, Yanshan University, Qinhuangdao 066004, China; ting0505ha@163.com (T.Z.); haoxiaohong2022@163.com (X.H.); wangyuefeng@ysu.edu.cn (Y.W.); chenchen@ysu.edu.cn (C.C.)

<sup>2</sup> National Engineering Research Center for Equipment and Technology of Cold Strip Rolling, Yanshan University, Qinhuangdao 066004, China

\* Correspondence: tswang@ysu.edu.cn

**Abstract:** In present study, a novel Nb-V microalloyed Fe–Mn–Al–C steel and a non-microalloyed Fe–Mn–Al–C austenitic steel were treated with different thermo-mechanical processes. The microstructure of the test steels was observed by scanning electron microscope, transmission electron microscope, electron probe micro-analyzer, and X-ray diffractometer. A tensile test was conducted to estimate the mechanical properties of the test steels. Results show that the equiaxed austenitic grains are obtained in both test steels, while hot rolling reduces the grain size significantly. The grain size of the Fe–Mn–Al–C steel decreases by 40%–55% after the addition of Nb-V due to the precipitation of nanoscale (Nb,V)C particles within the austenite matrix. Compared with the solid solution treated specimens, the strength of the hot-rolled or aged specimens is improved. Meanwhile, the strength of the Fe–Mn–Al–C steel with Nb-V microalloying is also increased by 55 MPa due to the precipitation strengthening and fine grain strengthening, while the elongation is decreased. The Nb-V microalloyed Fe–Mn–Al–C steel, after hot rolling + aging treatment, obtains the maximum strength, with the yield and tensile strength of 669 MPa and 1001 MPa, respectively. The strengthening mechanisms that contribute significantly to the yield strength are solid solution strengthening and dislocation strengthening. They are 185 MPa and 211 MPa, respectively, for the Nb-V microalloyed Fe–Mn–Al–C steel at hot rolling + aging conditions. Meanwhile, the segregation of carbon atoms after aging treatment also improves the yield strength significantly.

**Keywords:** Fe–Mn–Al–C austenitic steel; mechanical property; Nb-V microalloying; strengthening mechanisms; thermo-mechanical process



**Citation:** Zhao, T.; Hao, X.; Wang, Y.; Chen, C.; Wang, T. Influence of Thermo-Mechanical Process and Nb-V Microalloying on Microstructure and Mechanical Properties of Fe–Mn–Al–C Austenitic Steel. *Coatings* **2023**, *13*, 1513. <https://doi.org/10.3390/coatings13091513>

Academic Editors: Oana Catalina Mocioiu and Ana-Maria Mocioiu

Received: 14 July 2023

Revised: 18 August 2023

Accepted: 24 August 2023

Published: 27 August 2023



**Copyright:** © 2023 by the authors. Licensee MDPI, Basel, Switzerland. This article is an open access article distributed under the terms and conditions of the Creative Commons Attribution (CC BY) license (<https://creativecommons.org/licenses/by/4.0/>).

## 1. Introduction

Energy and environmental issues are becoming increasingly prominent. Due to these concerns, the use of low-density steel components in the automobile sector is getting increased attention. Fe–Mn–Al–C austenitic steel has a low density and excellent comprehensive mechanical properties [1,2]. This kind of steel includes 12%–30% Mn, 5%–12% Al, and 0.6%–2.0% C with mass fraction. The microstructure of Fe–Mn–Al–C austenitic steel after solid solution treatment is single austenite, short-range ordered structures, and precipitated phases uniformly distributed in the austenite matrix [3]. Due to the high content of alloying elements in the Fe–Mn–Al–C austenitic steel, such as C, Al, and Mn, solution strengthening plays an important role in its strength [4]. In addition, owing to the influence of precipitates in austenite grains on dislocation slip and arrangement during deformation, precipitation strengthening has become one of the most important strengthening mechanisms of Fe–Mn–Al–C austenitic steel [5].

The thermo-mechanical process plays a crucial role in the microstructure and mechanical properties of Fe–Mn–Al–C steel [6–10]. The effect of annealing temperature on

microstructural modification and tensile properties in an Fe-3.5Mn-5.8Al-0.35C lightweight steel was investigated by Sohn et al. [8]. The microstructure was composed of ferrite and austenite bands in a layered structure when the annealing temperature was higher than the dissolution finishing temperature of  $\kappa$ -carbides. With the increase in annealing temperature, the tensile strength increased gradually, while the yield strength and elongation decreased accordingly. This effect was mainly related to the reduction in mechanical and thermal stability of austenite with the increase in austenite grain size and volume fraction. Lee et al. [9] explored the microstructure and intrinsic mechanical behavior of an Fe-31.4Mn-11.4Al-0.89C steel after aging at 550 °C for various periods. The  $\beta$ -Mn phase nucleated at both ferrite/austenite phase boundaries and austenite grain boundaries after aging for 300 min and extended into the austenite grains by increasing aging time. The Vickers hardness increased dramatically after aging for 1000 min. Li et al. [10] analyzed the effect of rolling and subsequent aging treatments on microstructures and tensile properties of an Fe-23.38Mn-6.86Al-1.43C austenitic steel. They revealed that the average grain size decreased and strength significantly increased after hot rolling. The strength increased gradually by increasing the rolling reduction, with a decreased ductility, which was mainly related to the increment of dislocation density. The intragranular coarse  $\kappa$ -carbides in the hot-rolled test steel aged at 550 °C caused the increased strength and decreased ductility. These studies showed that varied thermo-mechanical processes develop different phase compositions, grain sizes, as well as the content and size of precipitates in Fe–Mn–Al–C steel, which could further affect mechanical properties.

In current research on precipitation strengthening,  $\kappa$ -carbide is the most intensive [11]. The effect of  $\kappa$ -carbides on the mechanical properties of Fe–Mn–Al–C austenitic steel is double-edged, mainly related to its size and distribution. Published studies have shown that fine intragranular  $\kappa$ -carbides can significantly improve the strength and hardness of Fe–Mn–Al–C austenitic steel. In contrast, coarse intergranular  $\kappa$ -carbides destroy plasticity and toughness [12,13]. The morphology and distribution of  $\kappa$ -carbides are mainly related to the alloying elements and thermo-mechanical processes [14]. Therefore, it is necessary to strictly control the alloy element content and treatment process parameters for Fe–Mn–Al–C austenitic steel, which restricts the production of Fe–Mn–Al–C austenitic steel. Research has stated that the addition of microalloying elements in Fe–Mn–Al–C steel can strengthen the austenitic matrix by forming highly stable carbides [15,16]. During the subsequent deformation process, precipitated carbides will hinder the dislocation movement, inhibit the growth of austenite grains, and finally produce precipitation strengthening and fine grain strengthening [17]. Meanwhile, these microalloying elements will preferentially combine with carbon atoms in the steel, reducing the precipitation driving force of  $\kappa$ -carbides and thereby preventing the detrimental effect of  $\kappa$ -carbides coarsening on mechanical properties [18]. For example, Zhou et al. [19] investigated the influence of Nb addition on the microstructure and mechanical properties of a hot-rolled Fe-8Mn-6Al-0.15C-0, 0.02Nb steel. The Nb-contained steel exhibited excellent mechanical properties, with tensile strength of 940 MPa and elongation of 36%, higher than the steel without Nb. The study showed that the addition of Nb led to the partitioning of C and Mn from austenite and retarded the  $\gamma/\alpha$  transformation. In addition, Zhang et al. [20] stated that V would promote the precipitation of Nb-enriched carbides at lower temperatures, which revealed that the combined addition of Nb and V could introduce better precipitation strengthening than an individual addition. However, limited research has been reported on the influences of Nb–V multi-microalloying on the microstructure and mechanical properties of Fe–Mn–Al–C austenitic steel.

The presented study investigates the mechanical properties under different thermo-mechanical processes in Nb–V multi-microalloyed Fe–Mn–Al–C austenitic steel by comparing it with the non-microalloyed one. The effect of Nb–V microalloying on the microstructure and mechanical properties of Fe–Mn–Al–C austenitic steel is analyzed.

## 2. Materials and Methods

The test steels used in the present study are low-density Fe–Mn–Al–C and Fe–Mn–Al–C–Nb–V austenitic steels, hereinafter referred to as ALDS and NbV-ALDS, respectively. The chemical composition of the test steels is given in Table 1. Both test steels were smelted in a vacuum induction furnace and then cast into ingots with approximately 100 mm diameter close to the riser, as shown in Figure 1. The ingots were homogenized at 1150 °C for 3 h and forged into rods with a diameter of 40 mm. The final forging temperature was above 850 °C. The thermo-mechanical process of the specimen after forging is shown in Figure 2. The forged specimen was solution treated at 1050 °C for 1 h, followed by water quenching. Then, it was aged at 550 °C for 5 h and finally air cooled. To improve the strength of the test steel, hot rolling deformation with a total reduction of 50% was conducted after solid solution at 1050 °C for 1 h, and water quenching was taken subsequently. The hot-rolled specimen was also aged at 550 °C for 5 h, followed by air cooling. In the description after, SS, SSA, HR, and HRA represent the solid solution, solid solution+ aging, hot rolling, and hot rolling + aging processes, respectively.

**Table 1.** Chemical composition of test steels (wt.%).

Test Steels	C	Al	Mn	Mo	Nb	V	S	P
ALDS	1.05	7.29	27.67	0.64	—	—	0.042	0.013
NbV-ALDS	1.05	7.33	27.92	0.62	0.16	0.16	0.037	0.014



**Figure 1.** Image of ingot prepared by induction vacuum furnace.

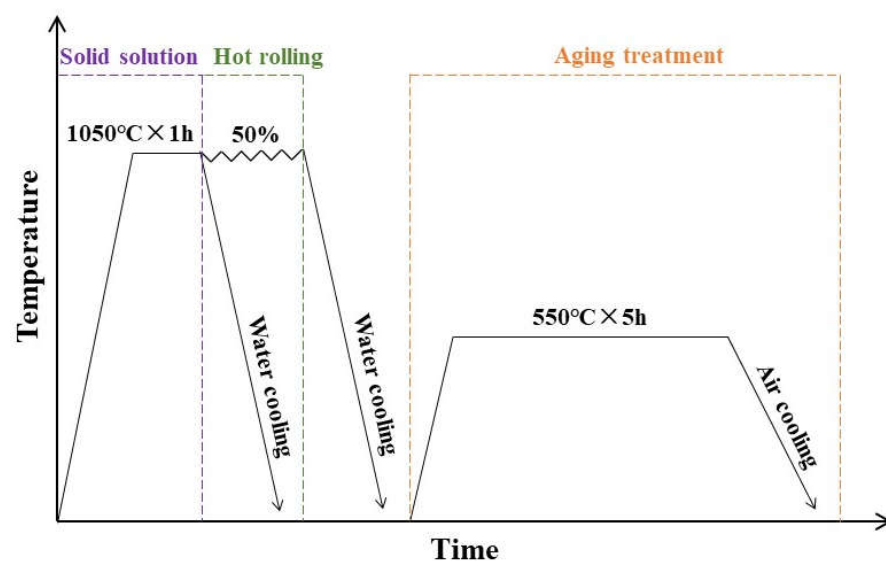


**Figure 2.** Schematic diagram of thermo-mechanical processes for test steel.

A tensile test was conducted on an MTS tensile testing machine following the ASTM E8M-16a standard with a strain rate of 3 mm/min. The picture of a tensile specimen is shown in Figure 3. The gauge diameter and length of the dog-bone-shaped tensile specimen were 5 mm and 25 mm, respectively, and the tensile direction was parallel to the forging or rolling direction. The tensile test was repeated three times with the same conditions. The microstructure of specimens treated by different thermo-mechanical processes was observed by scanning electron microscope (SEM, Hitachi SU5000, Hitachi, Tokyo, Japan), transmission electron microscope (TEM, Talos, F200X, FEI, Hillsboro, OR, USA), and electron probe micro-analyzer (EPMA, JXA-8530F, JEOL, Tokyo, Japan). The specimens for SEM and EPMA were mechanically polished using diamond paste after ground with waterproof abrasive papers (ranging from 150 to 1500) and then etched with 4 vol.% nitric acid alcohol solution. The working voltage, operating current, and working distance were 15 kV, 30 mA, and 5 mm, respectively, during SEM observation. In addition, the working voltage, operating current, and spot size during EPMA observation were 15 kV, 20 nA, and 1  $\mu\text{m}$ , respectively. The microstructure of the specimen was also analyzed by electron backscattered diffraction (EBSD) under the EDAX high-resolution probe equipped with SU-5000 SEM. The working voltage and scanning step while collecting the EBSD data were 20 kV and 0.5  $\mu\text{m}$ , respectively. The EBSD data were analyzed using OIM analysis software. EBSD specimens were cut into a thickness of approximately 0.6 mm by electrodischarging technique and then mechanically ground to  $\sim 30 \mu\text{m}$  by using waterproof abrasive papers. The thickness was decreased to perforation by a TenuPol-5 twin-jet electropolishing device at room temperature with an electrolyte of 10 vol.% perchloric acid alcohol solution under 19–20 V. The preparation scheme of TEM specimens was the same as that of EBSD, and the acceleration voltage was kept at 200 kV. A D/max-2500/PC X-ray diffractometer (XRD) with the diffraction source of Cu target  $K_{\alpha}$  radiation was used to measure the phase composition of the test steels. A  $\theta$ – $2\theta$  continuous scanning mode was used with the  $2\theta$  scanning speed of  $2^{\circ}/\text{min}$  and scanning range of  $40$ – $105^{\circ}$ .

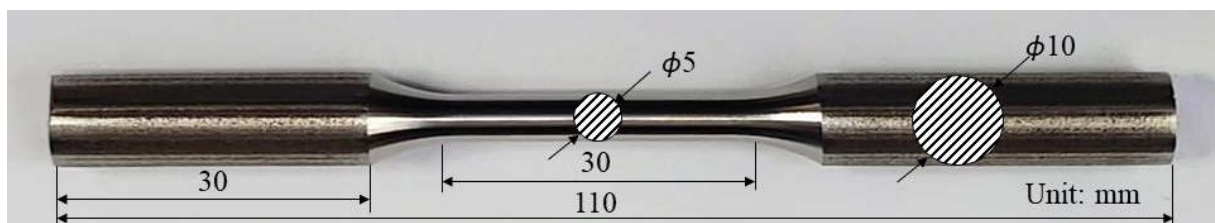


**Figure 3.** Image of bar tensile specimen.

### 3. Results

#### 3.1. Microstructure of the Test Steels Treated by Different Thermo-Mechanical Processes

The SEM images of the ALDS and NbV-ALDS treated by different thermo-mechanical processes are shown in Figures 4 and 5, respectively. By combining with the XRD patterns in Figure 6, it can be observed that the microstructure of both test steels after the solid solution is equiaxed austenite, and the grain size of the NbV-ALDS is finer than that of the ALDS. Figure 7 reveals the grain size distributions of test steels treated by different thermo-mechanical processes. The grain sizes of the ALDS after SS, SSA, HR, and HRA treatments are  $49.1 \pm 20.8 \mu\text{m}$ ,  $52.5 \pm 18.3 \mu\text{m}$ ,  $33.5 \pm 13.1 \mu\text{m}$ , and  $35.6 \pm 11.8 \mu\text{m}$ , respectively, while they are  $29.4 \pm 8.6 \mu\text{m}$ ,  $30.5 \pm 13.4 \mu\text{m}$ ,  $16.5 \pm 6.3 \mu\text{m}$ , and  $16.4 \pm 7.4 \mu\text{m}$ , respectively, for the NbV-ALDS. With the addition of Nb and V microalloying elements, the grain size decreases by 40%–55%. Meanwhile, the results show that the grain size of the test steels significantly reduces by 30%–45% after the hot rolling treatment and is slightly affected by the aging treatment.

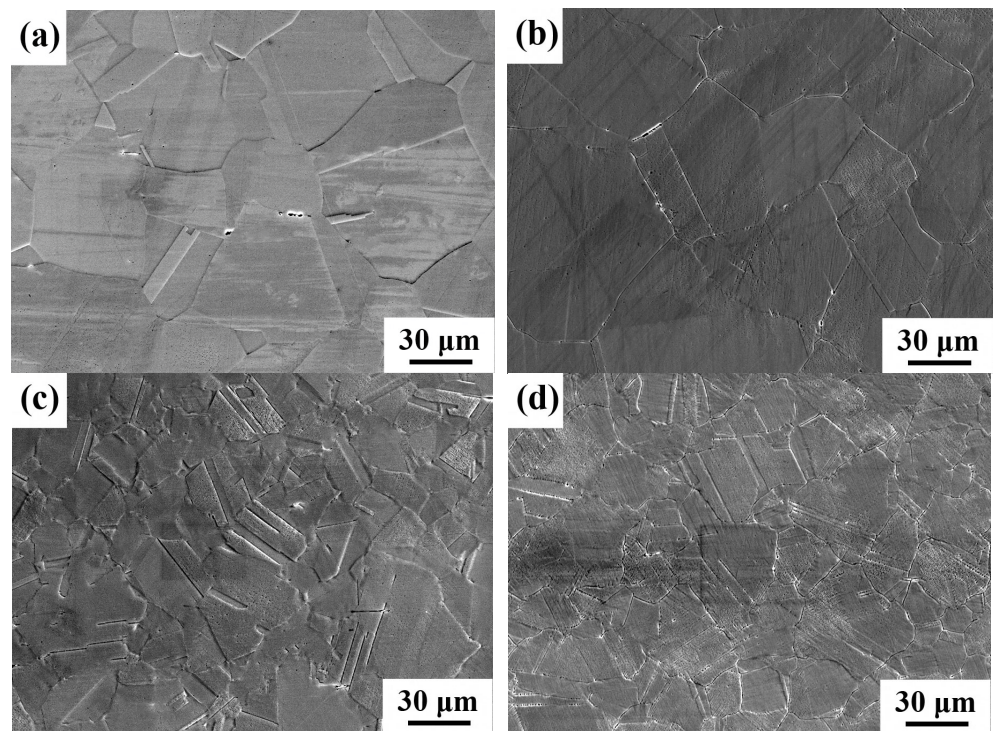


**Figure 4.** SEM images of ALDS treated by different thermo-mechanical processes. (a) SS, (b) SSA, (c) HR, (d) HRA.

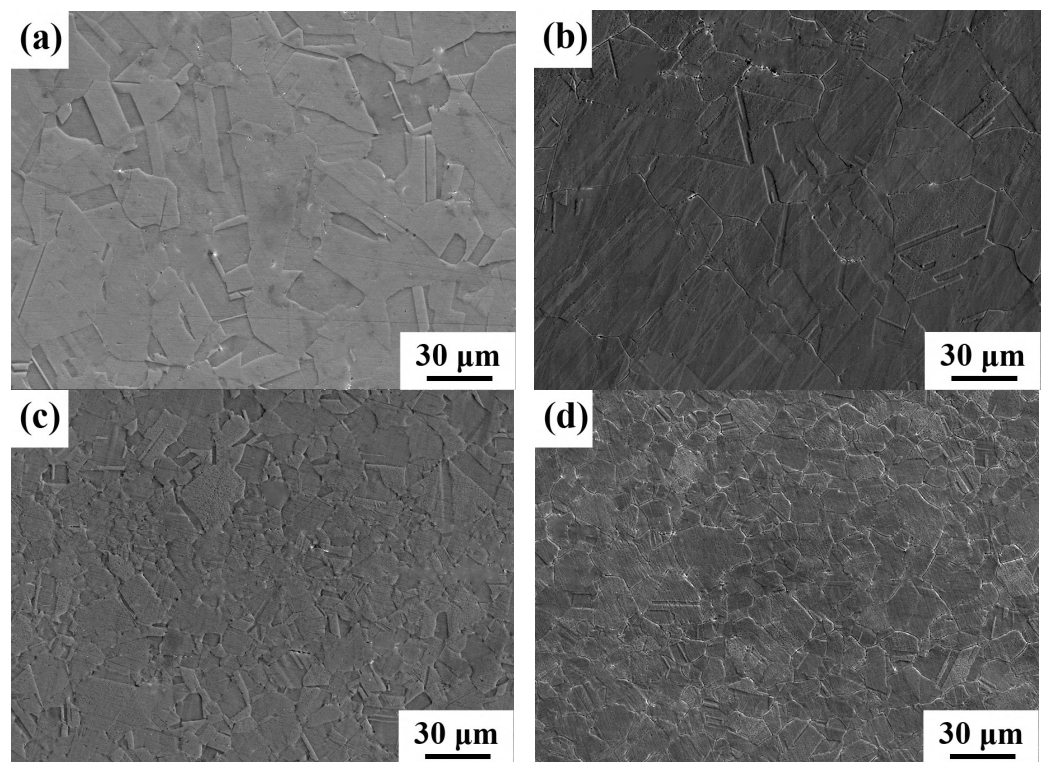


**Figure 5.** SEM images of NbV-ALDS treated by different thermo-mechanical processes. (a) SS, (b) SSA, (c) HR, (d) HRA.

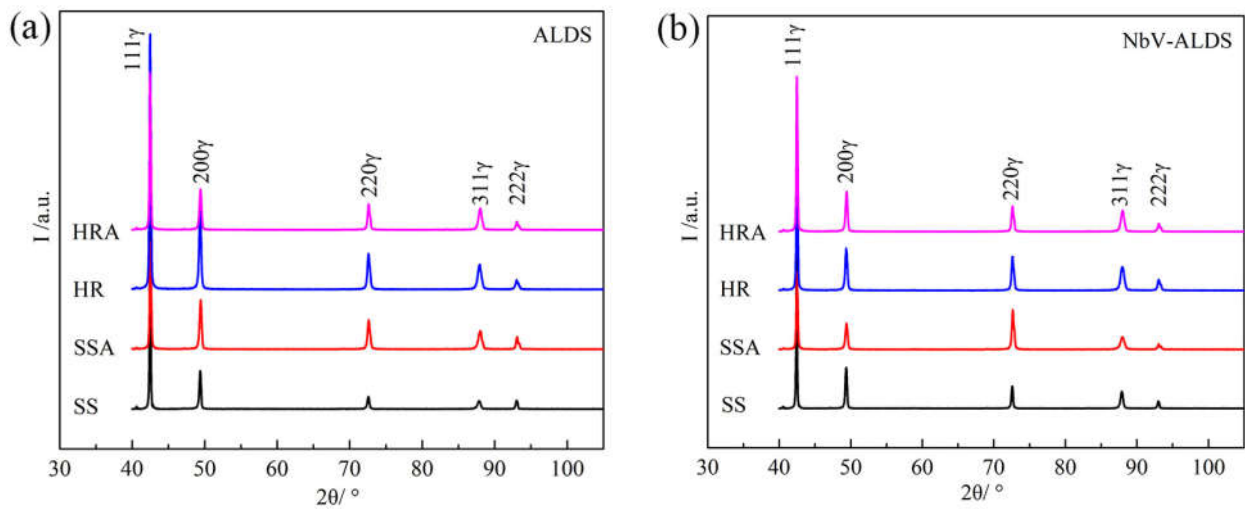


**Figure 6.** XRD patterns of ALDS (a) and NbV-ALDS (b) treated by different thermo-mechanical processes.

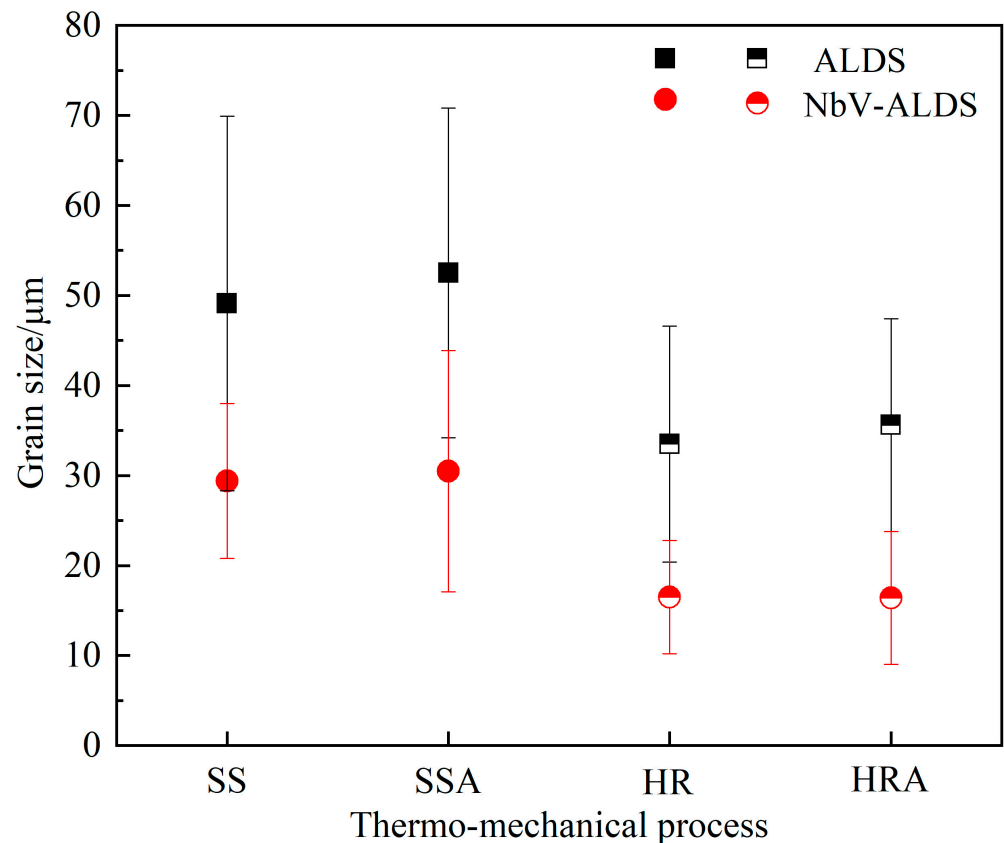


**Figure 7.** Grain size distributions of test steels treated by different thermo-mechanical processes.

The TEM images of the NbV-ALDS treated by different thermo-mechanical processes are shown in Figure 8. Several fine dispersed particles were found to precipitate in the austenitic matrix. The sizes of the precipitates in the NbV-ALDS after SS, SSA, HR, and HRA are  $82.9 \pm 29.7$  nm,  $96.9 \pm 59.7$  nm,  $77.4 \pm 24.3$  nm, and  $106.6 \pm 49.7$  nm, respectively, and the corresponding contents (area percentage) are determined to be 0.38%, 0.33%, 0.41%, and 0.40%, respectively. This means that the thermo-mechanical process hardly influences the content of precipitates. Hot rolling demonstrates a minimal effect on the size of precipitates, while it slightly increases after aging. The energy dispersive spectroscopy (EDS) maps and a high-resolution image of the precipitates shown in Figure 9 reveal that

the precipitated particles are (Nb,V)C with a face-centered cubic structure without any clear crystal orientation relationship with the austenite matrix. The addition of Nb-V leads to the formation of (Nb,V)C precipitates, and its pinning effect on grain boundaries makes the grains finer.

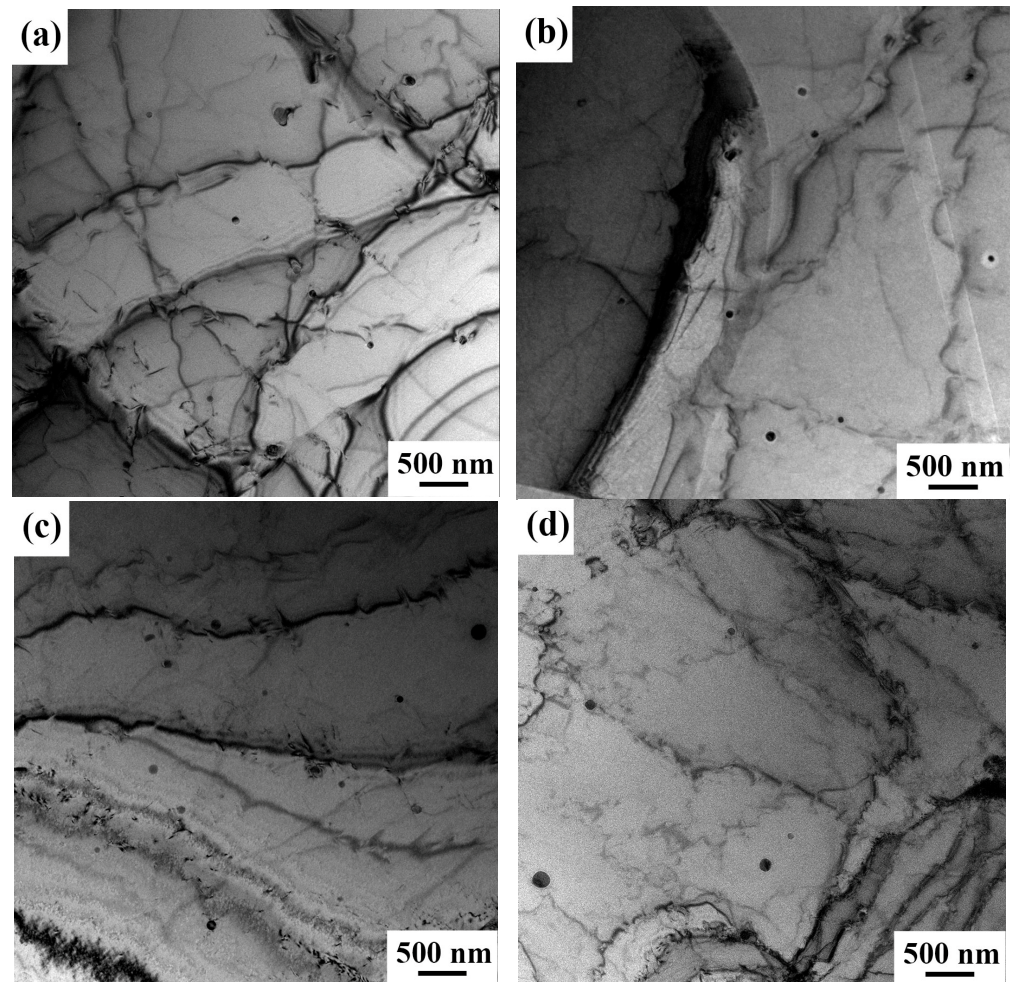


**Figure 8.** TEM images of NbV-ALDS treated by different thermo-mechanical processes. (a) SS, (b) SSA, (c) HR, (d) HRA.

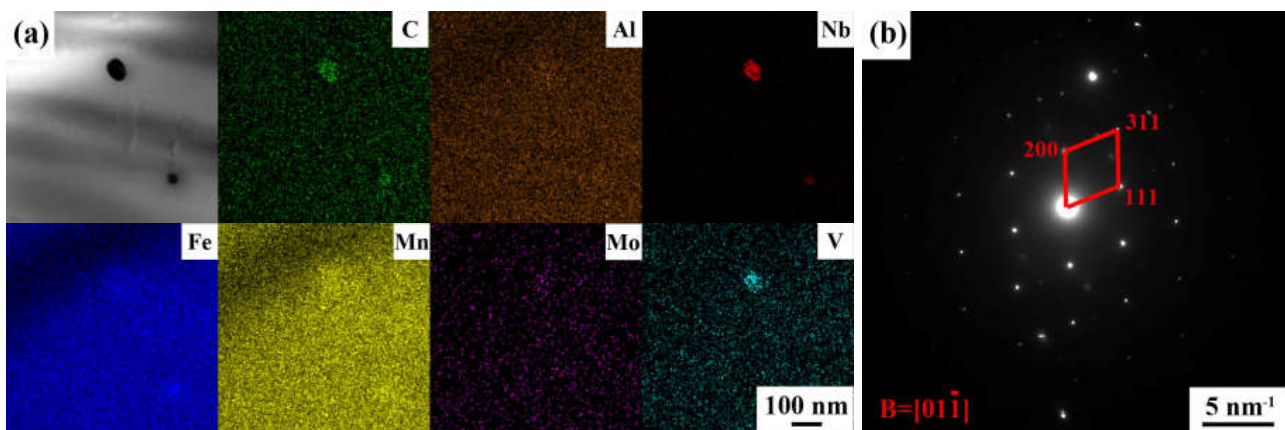


**Figure 9.** EDS maps (a) and corresponding selected area electron diffraction pattern (b) of the precipitates in NbV-ALDS treated by HRA.

### 3.2. Mechanical Properties of the Test Steels Treated by Different Thermo-Mechanical Processes

Figure 10 exhibits the engineering stress–engineering strain curves of the test steels treated by different thermo-mechanical processes. The detailed tensile properties are given in Table 2. Both steels show apparent continuous yielding during the tensile deformation process and ultimately undergo ductile fracture. The strength of the Fe–Mn–Al–C steel increases by 55 MPa after adding Nb–V, but the elongation decreases slightly at the same thermo-mechanical process. The test steels treated by HRA obtained the highest strength. In this condition, the yield, tensile strength, and elongation of the ALDS are 615 MPa, 966 MPa, and 54%, respectively, while those of the NbV-ALDS are 669 MPa, 1001 MPa, and 49%, respectively. The yield strength of the hot-rolled specimen increases by about 50 MPa compared with the solid solution-treated specimen, while the elongation is slightly decreased. Moreover, the aging treatment also improves the strength of the test steels. The yield strength of the ALDS and NbV-ALDS treated by SSA is 524 MPa and 561 MPa, respectively, which is higher than those of 452 MPa and 516 MPa treated by SS. These results show that aging treatment is more conducive to improving the yield strength than the tensile strength; hence, the yield ratio of the test steels increases after aging treatment.

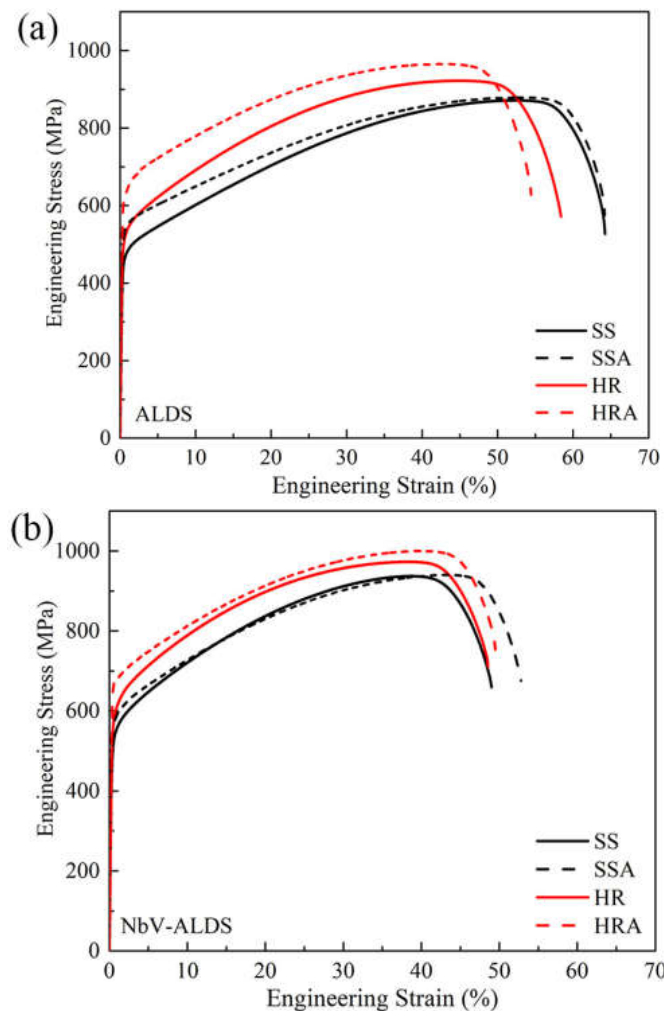


**Figure 10.** Engineering stress–engineering strain curves of ALDS (a) and NbV-ALDS (b) treated by different thermo-mechanical processes.

**Table 2.** Mechanical properties of test steels treated by different thermo-mechanical processes.

Test Steel	Thermo-Mechanical Process	Yield Strength (MPa)	Tensile Strength (MPa)	Yield Ratio	Elongation (%)
ALDS	SS	452	872	0.52	64.0
	SSA	524	879	0.60	63.7
	HR	503	923	0.54	58.2
	HRA	615	966	0.64	54.0

**Table 2.** Cont.

Test Steel	Thermo-Mechanical Process	Yield Strength (MPa)	Tensile Strength (MPa)	Yield Ratio	Elongation (%)
NbV-ALDS	SS	516	938	0.55	48.8
	SSA	561	940	0.60	52.4
	HR	574	973	0.59	48.0
	HRA	669	1001	0.67	49.0

Figures 11 and 12 show the EBSD maps of the test steels after tensile deformation. The color of the grain interior gradually changes, indicating the rotation of crystals. In the figures, the green lines are conventional high-angle grain boundaries, while those with red are coherent  $\Sigma 3$  boundaries. The equiaxed grains are significantly elongated because of tensile deformation. All grains exhibit the uni- or bidirectional strain markings, some passing through the entire grain and ending at the grain boundary, while others ending at the twin boundary [21].

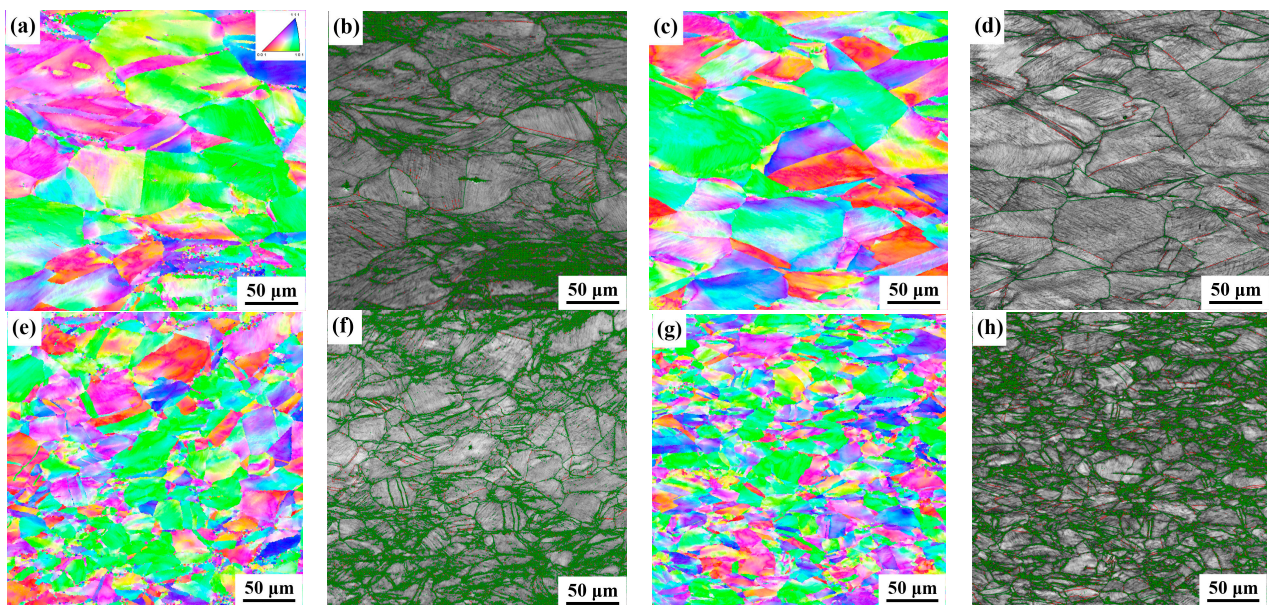


**Figure 11.** EBSD maps of ALDS treated by different thermo-mechanical processes after tensile deformation (green lines indicate conventional high-angle grain boundaries, and red lines are coherent  $\Sigma 3$  boundaries). (a) IPF map treated by SS, (b) IQ map treated by SS, (c) IPF map treated by SSA, (d) IQ map treated by SSA, (e) IPF map treated by HR, (f) IQ map treated by HR, (g) IPF map treated by HRA, (h) IQ map treated by HRA.

The TEM images of the NbV-ALDS after tensile deformation are shown in Figure 13. As can be seen in Figure 13a, the moving dislocation is inhibited by a (Nb,V)C precipitate during the deformation in the solid solution specimen. Classically, when moving dislocations are blocked by precipitates, there will be two types of interaction that occur. One

is called the shearing mechanism, that is, dislocations cut through the precipitates. The other is the bypass mechanism, where dislocations cannot pass through the precipitates but bypass them and form a dislocation loop around the precipitates [22]. The mechanism of interaction between dislocations and precipitates is mainly related to the size of the precipitates. It is a cutting mechanism when the size of the precipitates is small. However, it is a bypass mechanism with the size of the precipitates greater than  $40\ \mu$ . In the present study, due to the large size and high hardness of  $(\text{Nb},\text{V})\text{C}$ , dislocations can only bypass them; therefore, it is a bypass mechanism. Meanwhile, deformation microbands with small spacing are observed in the tensile-deformed specimens, as shown in Figure 13b. Some inhomogeneous entangled dislocations with high density are also observed in the deformation microbands. The locally sheared deformation bands with narrow band shapes are usually considered the second-generation microband [23]. The results indicate that the main plastic deformation mechanism in the Fe–Mn–Al–C steel is microband-induced plasticity. Figure 13c expresses the parallel arrangement of dislocation lines in the tensile-deformed NbV-ALDS after HRA treatment, which is a typical dislocation planer slip characteristic. The spacing of dislocation lines gradually becomes narrow along the direction indicated by the orange arrows.

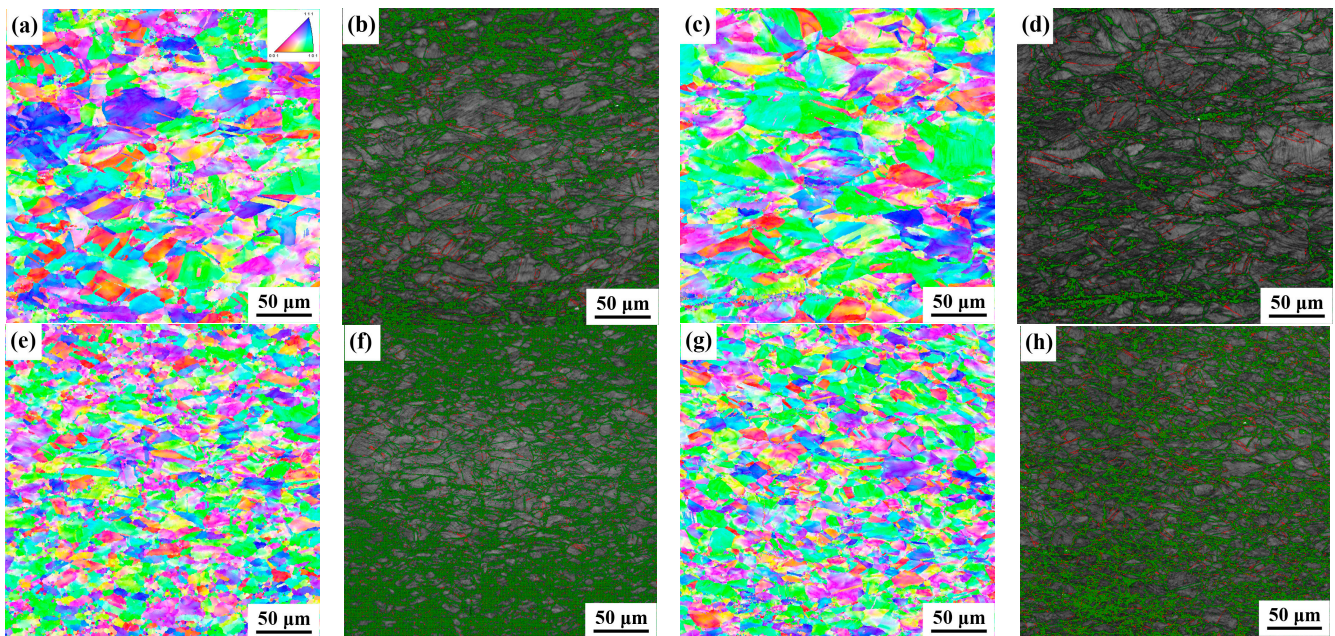


**Figure 12.** EBSD maps of NbV-ALDS treated by different thermo-mechanical processes after tensile deformation (green lines indicate conventional high-angle grain boundaries, and red lines are coherent  $\Sigma 3$  boundaries). (a) IPF map treated by SS, (b) IQ map treated by SS, (c) IPF map treated by SSA, (d) IQ map treated by SSA, (e) IPF map treated by HR, (f) IQ map treated by HR, (g) IPF map treated by HRA, (h) IQ map treated by HRA.

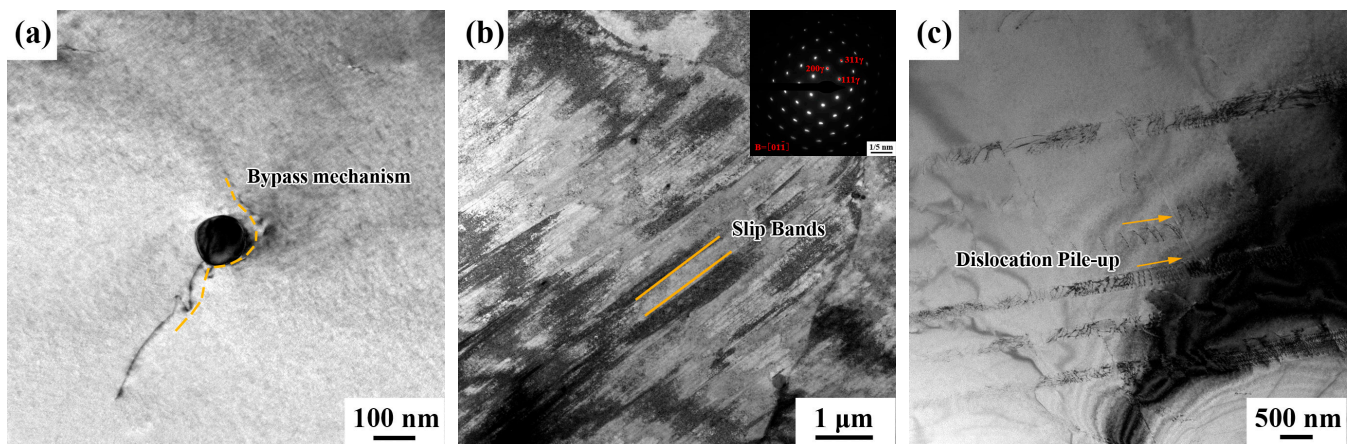


**Figure 13.** TEM images of tensile-deformed specimens of NbV-ALDS treated by different thermo-mechanical processes (a) SS, (b) SSA (the corresponding selected area electron diffraction is shown at the top-right corner of image), (c) HRA.

#### 4. Discussion

##### 4.1. Effect of the Thermo-Mechanical Process and Nb-V Microalloying on Microstructure and Tensile Deformation Behavior

Alloying and thermo-mechanical processes are two main factors that influence the microstructure of metal materials. The grain size of the Fe–Mn–Al–C steel is significantly reduced after adding the microalloying elements of Nb and V owing to the precipitation of nanoscale (Nb,V)C particles in the austenite matrix (Figure 8). The precipitated particles inhibit the growth of austenite grains [24], resulting in an apparent reduction in the grain size. Hot rolling also significantly reduces the grain size of both test steels, while aging treatment shows the least effect on the grain size (Figures 4 and 5). As reported, during the hot rolling process of the test steels, initial equiaxed grains are flattened or stretched along the rolling direction, forming elongated deformed bands. Meanwhile, the deformed grains undergo dynamic recrystallization, and refined equiaxed recrystallized grains are generated [25]. The grain of austenite is almost unchanged after aging treatment because the aging temperature is not high enough to exceed the recrystallization temperature of austenite. The size and content of the precipitated (Nb,V)C demonstrates an invisible change after hot rolling due to the high rolling temperature and short time. In comparison, the size of the precipitates slightly increases after aging treatment since there is a longer duration time.

Tensile deformation behavior is determined by the microstructure state [26]. As a result, the tensile curves present various characteristics in the test steels with different thermo-mechanical and microalloying treatments, as shown in Figure 10. To further analyze the deformation behavior, the strain-hardening rate curves of the test steels are calculated, as shown in Figure 14. It can be observed that the strain-hardening rate values of the test steels before fracture are positive, indicating that the plastic deformation is dominant by strain hardening. The variation behavior of the strain-hardening rate can be divided into three stages. The first is the sharp decrease stage (stage I), where the negative slope value of the curve is due to the development of moving dislocations and the saturation of dislocation stacks on the sliding surface [27]. After this, a rising and stable stage (stage II) of the strain-hardening rate starts, where the positive slope value of the curves is related to the formation and refinement of deformed microstructures such as unidirectional slip paths or Taylor lattices [21]. With further increasing the strain, the increased dislocation density improves the back stress worked on dislocation sources, which is caused by dislocation accumulation, leading to the depletion of the dislocation source and reduction in the strain-hardening rate. The curve of the strain-hardening rate tends to stabilize with a slope of around zero once the hardening effect by the deformation microstructure refinement is balanced with the softening effect by the depletion of the dislocation source. In the third

stage (stage III), with the development of necking and fracturing of the test steels, the deformation ends, and the strain-hardening rate drops sharply.

At the initial tensile deformation, the strain-hardening rate of specimens treated by hot rolling is higher than that of the solid solution-treated specimens. This is because the grain sizes of the specimens with hot rolling are smaller. The smaller grains have more grain boundaries, which are helpful in hindering the dislocation movement during the plastic deformation process; then, the work hardening rate will be improved and finally result in higher strength [28]. The work hardening rate of the NbV-ALDS is also higher than that of the ALDS. Besides the fine grain strengthening caused by the smaller grain size of the NbV-ALDS, the dislocation movement inhibited by the (Nb,V)C precipitates (Figure 11a) will also increase the working hardening rate [29]. Since the fine grain strengthening and precipitation strengthening effects, the strength of the test steels treated by HRA is the highest. Aging treatment reduces the working hardening rate; the reason will be discussed in the next section.

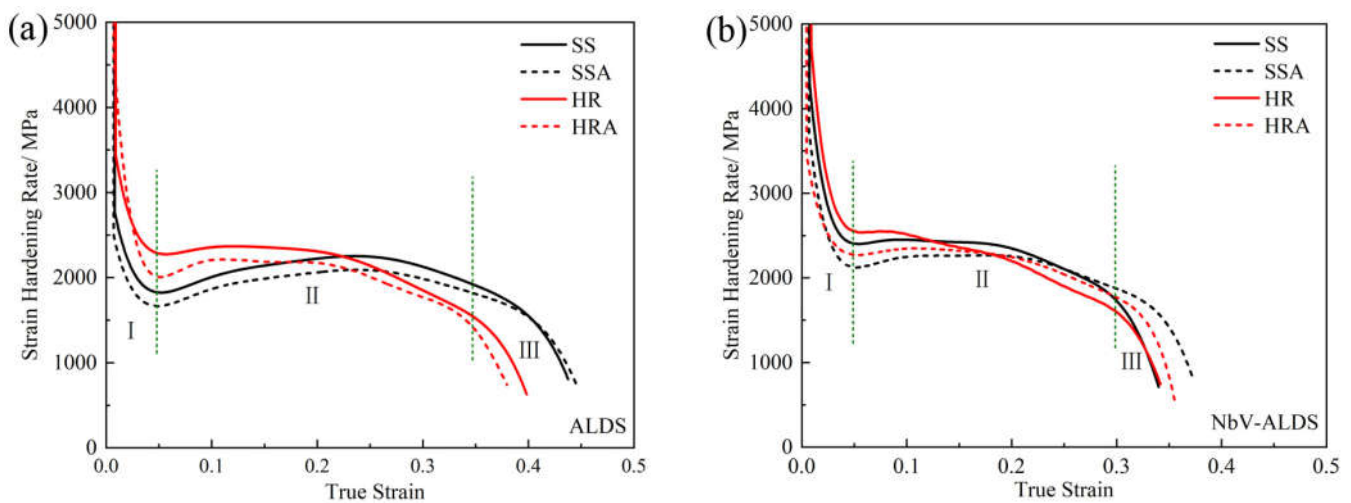


**Figure 14.** Strain-hardening rate of ALDS (a) and NbV-ALDS (b).

Generally, the deformation mechanism of fully austenitic steel is influenced by stacking fault energy (SFE). When the SFE is below 20 mJ/m<sup>2</sup>, it is a transformation-induced plasticity (TRIP) mechanism. Since the SFE gradually increases to 20~50 mJ/m<sup>2</sup>, the TWIP effect is the primary deformation mechanism. Besides, dislocation slip is the dominant deformation mechanism when the SFE is more than 50 mJ/m<sup>2</sup> [30]. According to the thermodynamic method, the SFEs of both test steels are ~77 mJ/m<sup>2</sup> at room temperature [31], indicating that the dislocation slip dominates during the deformation process. The microbands formed during tensile deformation (Figures 11 and 12) can increase dislocation density, resulting in the rise of the work hardening rate, thus making the microband-induced plasticity the principal deformation mechanism in the test steels.

#### 4.2. Contribution of Various Strengthening Effects to the Yield Strength

The mechanical properties of the test steels are determined by their microstructures. No systematic research has yet shown the effect of various microstructure parameters on yield strength in Fe–Mn–Al–C steel. The strengthening effects in Fe–Mn–Al–C steel mainly include solid solution strengthening, fine grain strengthening, precipitation strengthening, and dislocation strengthening. The strengthening model can evaluate the relevant strengthening mechanism based on dislocation density and precipitates [32]. Therefore, quantitative analysis is essential to determine the influence of microstructure on yield strength and provide guidance for the production of Fe–Mn–Al–C steel. According to the strengthening model, yield strength can be expressed as follows:

$$\sigma_y = \sigma_0 + \sigma_{ss} + \sigma_{gb} + \sigma_p + \sigma_d \quad (1)$$

where  $\sigma_y$  is yield strength,  $\sigma_0$  is the friction stress, and  $\sigma_{ss}$ ,  $\sigma_{gb}$ ,  $\sigma_p$ , and  $\sigma_d$  are the contributions of solid solution strengthening, grain boundary strengthening, precipitation strengthening, and dislocation strengthening, respectively. The different strength contributions are discussed as follows.

(1) Lattice friction stress

Lattice friction is the force that the lattice blocks the movement of dislocations. The lattice friction stress of the test steels can be calculated by the following expression [33].

$$\sigma_0 = \sqrt{3}\tau_0 \quad (2)$$

where  $\sigma_0$  is the friction stress of lattice,  $\tau_0$  is the shear stress of dislocation movement, and  $\tau_0 = 2 \times 10^{-4}G$ ,  $G$  is the shear modulus (68 GPa) [34]. Using these parameters, the lattice friction stress of the test steels is 23.6 MPa.

(2) Solid solution strengthening

Solid solution strengthening depends on the volume fraction of alloy elements dissolved in the matrix. The solid solution of Nb and V microalloying elements in the NbV-ALDS is neglected. The following empirical formula is used to calculate the contribution of solid solution strengthening in Fe–Mn–Al–C steels [35].

$$\sigma_{ss} = 4570[C] + 37[Mn] + 1754[Al] + 11[Mo] \quad (3)$$

where  $\sigma_{ss}$  is the contribution of a solid solution to yield strength, and  $[i]$  is the mass fraction of the alloying element.

(3) Grain boundary strengthening

Theoretically, the finer the grain size, the higher the strength of the steels. This is because the finer grains contain more grain boundaries within the microstructure, hindering dislocation movement and producing dislocation pile-up during the plastic deformation process when deformed and subjected to external forces. For plastic deformations, it is necessary to increase the external force to improve the strength of materials. The contribution of the grain boundary strengthening calculated based on the Hall–Petch relationship is given by [36].

$$\sigma_{gb} = k/\sqrt{d} \quad (4)$$

where  $k$  is a constant, i.e., 14.55 MPa·mm<sup>1/2</sup> [37], and  $d$  is the average grain size. The contribution of grain boundary strengthening is given in Table 3.

(4) Precipitation strengthening

Since the nanosized (Nb,V)C particles precipitated in Fe–Mn–Al–C steels after Nb–V addition uniformly distribute on the austenite matrix, those become the obstacle of dislocation slipping and hinder the movement of dislocations. The interaction between precipitates and dislocations causes a substantial improvement in yield strength in Fe–Mn–Al–C steel. Scott et al. [38] studied the addition of microalloying elements Ti, Nb, and V into high-manganese steel. There were TiC, NbC, and VC particles precipitated in the matrix after heat treatment, which refined the microstructure of high-manganese steel and improved the yield strength due to a combined effect of the fine grain strengthening and precipitation strengthening compared with the high-manganese steel without microalloying. The precipitation strengthening of the test steels can be expressed as follows [39].

$$\sigma_p = 9.549 \times 10^3 \frac{f^{1/2}}{d_p} \ln(20.417d_p) \quad (5)$$

where  $\sigma_p$  is the contribution of precipitation strengthening,  $f$  is the volume fraction of precipitates in the austenitic matrix, and  $d_p$  is the average size of the precipitates.

## (5) Dislocation strengthening

During the plastic deformation, dislocations slip, resulting in interactions. Plastic deformation is difficult because the slip dislocations are inhibited by tangled dislocations, thereby improving the strength of the materials. The dislocation strengthening of the test steel is calculated according to Equation (6) [40].

$$\sigma_d = M\alpha Gb\rho^{\frac{1}{2}} \quad (6)$$

where  $\sigma_d$  is the contribution of precipitation strengthening,  $M$  is Taylor factor (3.06 when the material is entirely austenite),  $\alpha$  is a geometric factor (0.136) [41],  $G$  is shear modulus,  $b$  is Burgers vector, and  $\rho$  is dislocation density.

The dislocation density of the test steel is analyzed through XRD and is calculated by Equation (7) [42].

$$\rho = \frac{2\sqrt{3}(\varepsilon^2)^{\frac{1}{2}}}{db} \quad (7)$$

where  $\rho$  is dislocation density,  $(\varepsilon^2)^{\frac{1}{2}}$  is average lattice strain,  $d$  is the size of the coherent diffraction zone, and  $b$  is Burgers vector.

The contributions of five strengthening mechanisms to yield strength are displayed in Table 3. The comparison of these values with the experimental yield strength is shown in Figure 15. It can be found that the calculated yield strength of the test steels treated by solid solution and hot rolling treatment is close to the actual experimental yield strength, indicating that the calculation method and parameters selected are correct. The strengthening mechanisms that contribute significantly to the yield strength are solid solution and dislocation strengthening. However, there is a gap of about 100 MPa between the calculated yield strength and actual yield strength for the test steels treated by aging treatment. Therefore, it is necessary to explore the evolution in the microstructure of the test steel before and after aging treatments to clarify the additional strengthening effect.

**Table 3.** Contribution of different strengthening effects to yield strength.

Test Steel	Thermo-Mechanical Process	$\sigma_0$	$\sigma_{ss}$	$\sigma_{gb}$	$\sigma_p$	$\sigma_d$	$\sigma_y$ -Calculated
ALDS	SS	23.6	183.9	65.7	0	173.5	446.7
	SSA	23.6	183.9	63.5	0	141.6	412.6
	HR	23.6	183.9	79.5	0	220.5	507.5
	HRA	23.6	183.9	77.1	0	210.0	494.6
NbV-ALDS	SS	23.6	184.7	84.9	52.8	178.1	524.1
	SSA	23.6	184.7	83.3	43.0	154.6	489.2
	HR	23.6	184.7	113.3	58.2	206.4	586.2
	HRA	23.6	184.7	113.6	43.5	211.3	576.7

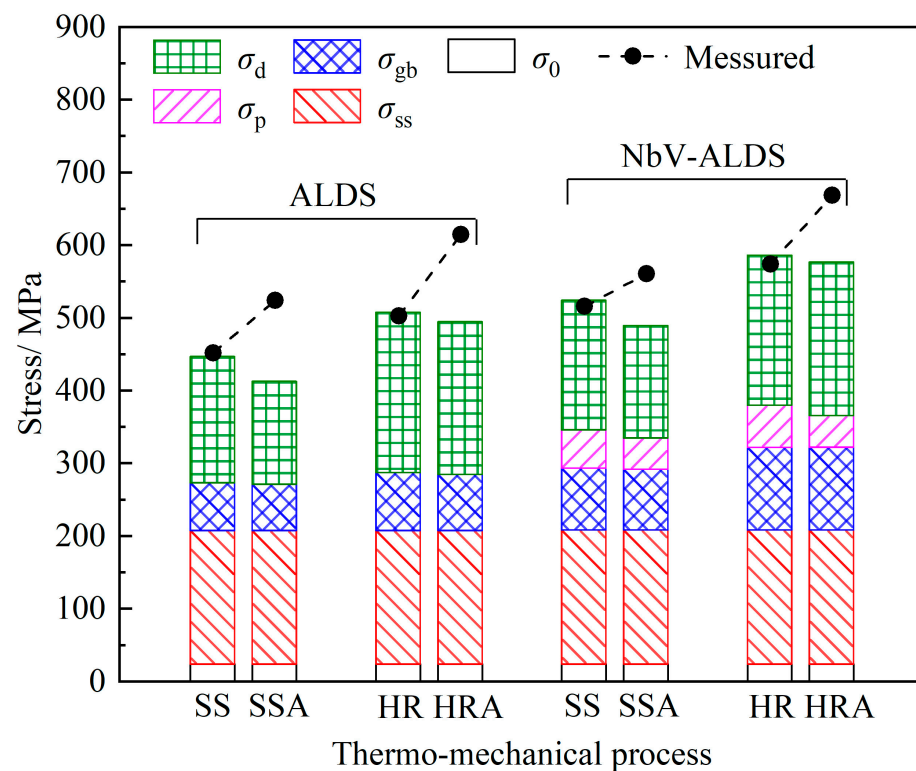


**Figure 15.** Comparison of the sum of contributions to yield strength of the strengthening mechanism with the experimental strength.

EPMA was used to analyze the specimens of the ALDS and NbV-ALDS treated by solid solution and aging treatment. The results are shown in Figures 16 and 17. The distribution of carbon elements in the test steels treated by aging differed from those treated with a solid solution. The distribution of carbon atoms in the specimens treated by solid solution is relatively uniform in the grain interior or at the grain boundaries. In comparison, the carbon atoms after aging treatment show some segregation phenomenon at grain boundaries, annealed twin boundaries, and (Nb,V)C precipitates. During the aging process, surplus vacancies in the quenched or hot-rolled specimens will gradually be annihilated, and as the aging time prolongs, the segregation of carbon atoms will be aggravated [43]. The segregation of carbon atoms could hinder the dislocation movement and pin dislocations during plastic deformation. It restrains the dislocation relaxation at the grain boundary, improving the strength of the test steels [44,45]. The increase in the content of the carbon atoms at grain boundaries also improves the plastic deformation stress; thus, the strength of the test steels is enhanced [46], and the yield strength of the test steels after aging treatment is significantly increased. For the NbV-ALDS, the addition of Nb-V will reduce vacancies in the specimens and thus reduce the segregation of carbon atoms [43]; on the other hand, the precipitated (Nb,V)C particles will intensify the segregation of carbon atoms. The difference value between the calculated and actual experimental yield strength of the NbV-ALDS treated by aging is smaller than that of the ALDS, indicating that the Nb-V microalloying will diminish the segregation phenomenon of carbon atoms, which is consistent with the test results (Figures 16d and 17d). However, the segregation of carbon atoms towards the grain boundary also causes the concentration of carbon in the austenite matrix to decrease the strain-hardening rate of the test steels. Therefore, there is a minor increase in the tensile strength of the test steels compared with the yield strength (Figure 10), which leads to a larger yield strength ratio after aging treatment.

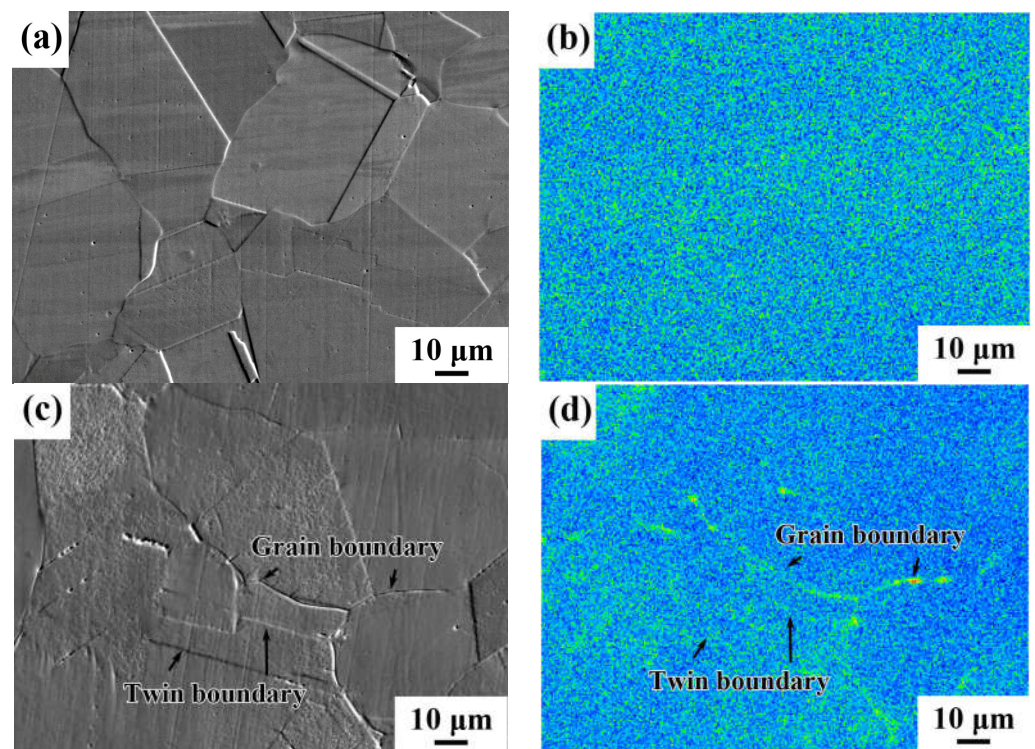


**Figure 16.** EPMA maps of ALDS treated by different thermo-mechanical processes. (a) SS, (b) distribution map of carbons in (a), (c) SSA, (d) distribution map of carbons in (c).

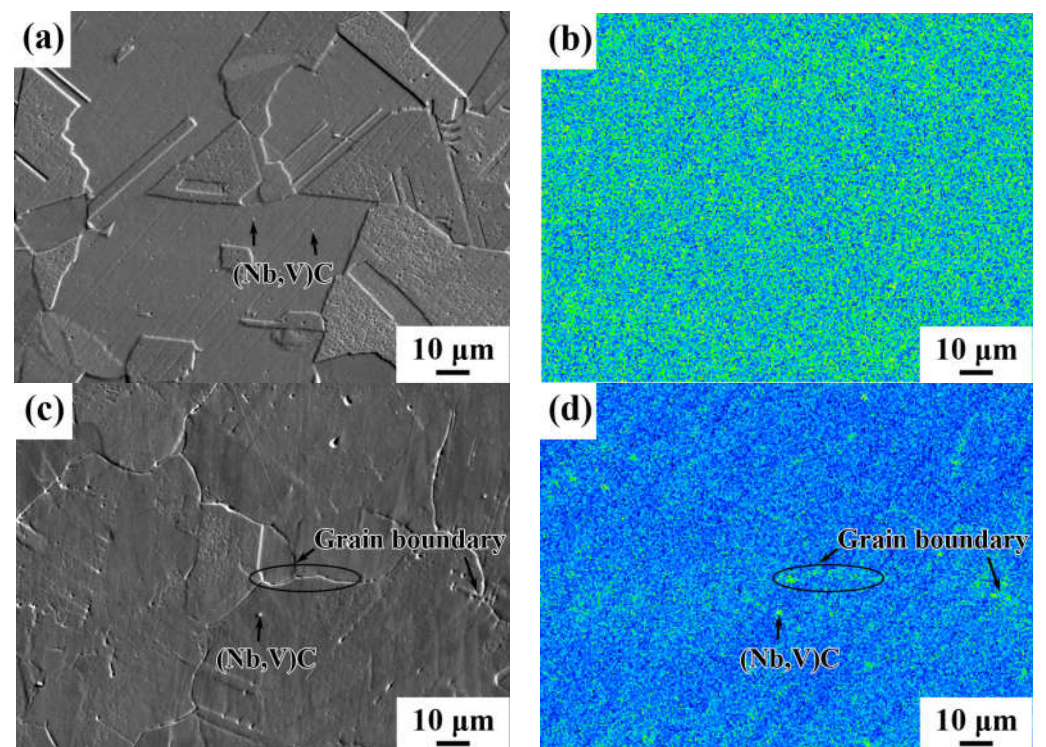


**Figure 17.** EPMA maps of NbV-ALDS treated by different thermo-mechanical processes. (a) SS, (b) distribution map of carbons in (a), (c) SSA, (d) distribution map of carbons in (c).

## 5. Conclusions

The microstructure and mechanical properties of the ALDS and NbV-ALDS treated by different thermo-mechanical processes are analyzed and compared. The main conclusions of this study are as follows:

- (1) Hot rolling significantly reduces the austenitic grain size of both test steels by 30%–45%. The grain size of the NbV-ALDS decreases by 40%–55% compared with that of the ALDS at the same thermo-mechanical process since the precipitation of nanoscale (Nb,V)C particles inhibits the growth of austenite grains. The (Nb,V)C particles hardly change in size and content during high temperature and hot rolling treatment because of their high thermal stability.
- (2) The strength of the test steels treated by hot rolling or aging is improved. The strength of the Fe–Mn–Al–C steel with Nb–V microalloying increases by 55 MPa due to the precipitation strengthening and fine grain strengthening of (Nb,V)C particles. However, the elongation is decreased. The test steels, after hot rolling + aging treatment, obtain the maximum strength. The yield and tensile strength of the ALDS are 615 MPa and 966 MPa, respectively, while the yield and tensile strength of the NbV-ALDS are 669 MPa and 1001 MPa, respectively.
- (3) The strengthening mechanisms contributing appreciably to the yield strength are solid solution and dislocation strengthening. These strengthening effects contribute 185 MPa and 211 MPa, respectively, to the yield strength for the NbV-ALDS steel after hot rolling + aging treatment. The segregation of carbon atoms to boundaries during aging also improves the yield strength of the test steels. The primary deformation mechanism is microband induced plasticity.
- (4) The addition of forceful carbide-forming microalloying elements is expected to become the focus of research in the Fe–Mn–Al–C austenitic low-density steel field, utilizing the advantages of fine precipitates. It is recommended to optimize the chemical composition of microalloyed Fe–Mn–Al–C austenitic steel and explore its various application properties, such as magnetism, corrosion resistance, fatigue, and wear properties, in future studies.

**Author Contributions:** T.Z.: Conceptualization, Formal analysis, Investigation, Data curation, Writing—original draft, Preparation, Writing—review and editing, and Visualization. X.H.: Methodology and Preparation. Y.W.: Data curation. C.C.: Writing—review and editing and Funding support. T.W.: Conceptualization, Supervision, and Writing—review and editing. All authors have read and agreed to the published version of the manuscript.

**Funding:** The authors gratefully acknowledge the National Natural Science Foundation of China (52201143), the Science and Technology Project of Hebei Education Department (BJK2023033), and the Hebei Province Innovation Ability Promotion Project (22567609H).

**Institutional Review Board Statement:** The author confirms that the manuscript is not under review or published elsewhere. The author states that the research was conducted according to ethical standards. There is no ethical concern.

**Informed Consent Statement:** Not applicable.

**Data Availability Statement:** All data generated or analyzed during this study are included in this published article.

**Conflicts of Interest:** The authors declare that they have no known competing financial interest or personal relationships that could have appeared to influence the work reported in this paper.

## References

1. Frommeyer, G.; Brück, U.; Neumann, P. Supra-ductile and high-strength manganese-TRIP/TWIP steels for high energy absorption purposes. *ISIJ Int.* **2003**, *43*, 438–446. [[CrossRef](#)]
2. Kim, H.; Suh, D.W.; Kim, N.J. Fe–Al–Mn–C lightweight structural alloys: A review on the microstructures and mechanical properties. *Sci. Technol. Adv. Mater.* **2013**, *14*, 014205. [[CrossRef](#)]

3. Chen, S.; Rana, R.; Haldar, A.; Ray, R.K. Current state of Fe-Mn-Al-C low density steels. *Prog. Mater. Sci.* **2017**, *89*, 345–391. [[CrossRef](#)]
4. Chang, K.M.; Chao, C.G.; Liu, T.F. Excellent combination of strength and ductility in a Fe-9Al-28Mn-1.8C alloy. *Scr. Mater.* **2010**, *63*, 162–165. [[CrossRef](#)]
5. Gutierrez-Urrutia, I.; Raabe, D. Influence of Al content and precipitation state on the mechanical behaviour of austenitic high-Mn low-density steels. *Scr. Mater.* **2013**, *68*, 343–347. [[CrossRef](#)]
6. Chen, Z.; Liu, M.-X.; Zhang, J.-K.; Yang, L.; Zhang, Y.-H.; Song, C.-J.; Zhai, Q.-J. Effect of annealing treatment on microstructures and properties of austenite-based Fe-28Mn-9Al-0.8C lightweight steel with addition of Cu. *China Foundry* **2021**, *18*, 207–216. [[CrossRef](#)]
7. He, W.; Wang, B.-L.; Yang, Y.; Zhang, Y.-H.; Duan, L.; Luo, Z.-P.; Song, C.-J.; Zhai, Q.-J. Microstructure and mechanical behavior of a low-density Fe-12Mn-9Al-1.2C steel prepared using centrifugal casting under near-rapid solidification. *J. Iron Steel Res. Int.* **2018**, *25*, 830–838. [[CrossRef](#)]
8. Sohn, S.S.; Lee, B.-J.; Lee, S.; Kim, N.J.; Kwak, J.-H. Effect of annealing temperature on microstructural modification and tensile properties in 0.35C-3.5Mn-5.8Al lightweight steel. *Acta Mater.* **2013**, *61*, 5050–5066. [[CrossRef](#)]
9. Lee, K.; Park, S.-J.; Lee, J.; Moon, J.; Kang, J.-Y.; Kim, D.-I.; Suh, J.-Y.; Han, H.N. Effect of aging treatment on microstructure and intrinsic mechanical behavior of Fe-31.4Mn-11.4Al-0.89C lightweight steel. *J. Alloys Compd.* **2016**, *656*, 805–811. [[CrossRef](#)]
10. Li, Z.; Wang, Y.; Cheng, X.; Li, Z.; Gao, C.; Li, S. The effect of rolling and subsequent aging on microstructures and tensile properties of a Fe-Mn-Al-C austenitic steel. *Mater. Sci. Eng. A* **2021**, *822*, 141683. [[CrossRef](#)]
11. Lu, W.J.; Zhang, X.F.; Qin, R.S.  $\kappa$ -carbide hardening in a low-density high-Al high-Mn multiphase steel. *Mater. Lett.* **2015**, *138*, 96–99. [[CrossRef](#)]
12. Jeong, S.; Park, G.; Kim, B.; Moon, J.; Park, S.-J.; Lee, C. Precipitation behavior and its effect on mechanical properties in weld heat affected zone in age hardened FeMnAlC lightweight steels. *Mater. Sci. Eng. A* **2019**, *742*, 61–68. [[CrossRef](#)]
13. Zhang, G.F.; Shi, H.Y.; Wang, S.T.; Tang, Y.H.; Zhang, X.Y.; Jing, Q.; Liu, R.P. Ultrahigh strength and high ductility lightweight steel achieved by dual nanoprecipitate strengthening and dynamic slip refinement. *Mater. Lett.* **2023**, *330*, 133366. [[CrossRef](#)]
14. Haase, C.; Zehnder, C.; Ingendahl, T.; Bikar, A.; Tang, F.; Hallstedt, B.; Hu, W.P.; Bleck, W.; Molodov, D.A. On the deformation behavior of k-carbide-free and k-carbide containing high-Mn light-weight steel. *Acta Mater.* **2017**, *122*, 332–343. [[CrossRef](#)]
15. Li, Z.; Wang, Y.C.; Cheng, X.W.; Li, Z.Y.; Du, J.K.; Li, S.K. The effect of Ti-Mo-Nb on the microstructures and tensile properties of a Fe-Mn-Al-C austenitic steel. *Mater. Sci. Eng. A* **2020**, *780*, 139220. [[CrossRef](#)]
16. Salas-Reyes, A.E.; Mejía, I.; Bedolla-Jacuinde, A.; Boulaajaj, A.; Calvo, J.; Cabrera, J.M. Hot ductility behavior of high-Mn austenitic Fe-22Mn-1.5Al-1.5Si-0.45C TWIP steels microalloyed with Ti and V. *Mater. Sci. Eng. A* **2014**, *611*, 77–89. [[CrossRef](#)]
17. Gwon, H.; Kim, J.-K.; Shin, S.; Cho, L.; De Cooman, B.C. The effect of vanadium micro-alloying on the microstructure and the tensile behavior of TWIP steel. *Mater. Sci. Eng. A* **2017**, *696*, 416–428. [[CrossRef](#)]
18. Ma, T.; Li, H.R.; Gao, J.X.; Wang, X.F.; Song, H.W.; Li, Y.G. Progress on strengthening mechanism and tensile properties of Fe-Mn-Al-C low density steel and prospect of Nb microalloying. *Mater. Rep.* **2020**, *34*, 23154–23164.
19. Zhou, N.P.; Song, R.B.; Song, R.F.; Li, X.; Li, J.J. Influence of Nb addition on microstructure and mechanical properties of medium-Mn low-density steels. *Steel Res. Int.* **2018**, *89*, 1700552. [[CrossRef](#)]
20. Zhang, Y.H.; Tong, Q.G.; Liu, Y.S. Effect of rolling process parameters on precipitation strengthening of V and Nb microalloyed steel. *J. Northeast Univ. Technol.* **1992**, *13*, 363–367.
21. Yoo, J.D.; Park, K.T. Microband-induced plasticity in a high Mn-Al-C light steel. *Mater. Sci. Eng. A* **2008**, *496*, 417–424. [[CrossRef](#)]
22. Fu, J.; Li, G.; Mao, X.; Fang, K. Nanoscale cementite precipitates and comprehensive strengthening mechanism of steel. *Metall. Mater. Trans. A* **2011**, *42*, 3797–3812. [[CrossRef](#)]
23. Park, K.T. Tensile deformation of low-density Fe-Mn-Al-C austenitic steels at ambient temperature. *Scr. Mater.* **2013**, *68*, 375–379. [[CrossRef](#)]
24. Zhao, T.; Rong, S.; Hao, X.; Wang, Y.; Chen, C.; Wang, T. Effect of Nb-V microalloying on hot deformation characteristics and microstructures of Fe-Mn-Al-C austenitic steel. *Mater. Charact.* **2022**, *183*, 111595. [[CrossRef](#)]
25. Castan, C.; Montheillet, F.; Perlade, A. Dynamic recrystallization mechanisms of an Fe-8% Al low density steel under hot rolling conditions. *Scr. Mater.* **2013**, *68*, 360–364. [[CrossRef](#)]
26. Yang, F.Q.; Song, R.B.; Li, Y.P.; Sun, T.; Wang, K.K. Tensile deformation of low density duplex Fe-Mn-Al-C steel. *Mater. Design* **2015**, *76*, 32–39. [[CrossRef](#)]
27. Ji, F.; Song, W.; Ma, Y.; Li, C.; Bleck, W.; Wang, G. Recrystallization behavior in a low-density high-Mn high-Al austenitic steel undergone thin strip casting process. *Mater. Sci. Eng. A* **2018**, *733*, 87–97. [[CrossRef](#)]
28. Dini, G.; Najafzadeh, A.; Ueji, R.; Monir-Vaghefi, S. Tensile deformation behavior of high manganese austenitic steel: The role of grain size. *Mater. Des.* **2010**, *31*, 3395–3402. [[CrossRef](#)]
29. Rao, M.P.; Sarma, V.S.; Sankaran, S. Development of high strength and ductile ultra fine grained dual phase steel with nano sized carbide precipitates in a V-Nb microalloyed steel. *Mater. Sci. Eng. A* **2013**, *568*, 171–175. [[CrossRef](#)]
30. Park, K.-T.; Kim, G.; Kim, S.K.; Lee, S.W.; Hwang, S.W.; Lee, C.S. On the transitions of deformation modes of fully austenitic steels at room temperature. *Met. Mater. Int.* **2010**, *16*, 1–6. [[CrossRef](#)]
31. Zambrano, O.A. Stacking fault energy maps of Fe-Mn-Al-C-Si steels: Effect of temperature, grain size, and variations in compositions. *J. Eng. Mater. Technol.* **2016**, *138*, 041010. [[CrossRef](#)]

32. Park, D.-B.; Huh, M.-Y.; Shim, J.-H.; Suh, J.-Y.; Lee, K.-H.; Jung, W.-S. Strengthening mechanism of hot rolled Ti and Nb microalloyed HSLA steels containing Mo and W with various coiling temperature. *Mater. Sci. Eng. A* **2013**, *560*, 528–534. [[CrossRef](#)]
33. Pavel, K.; Andrey, B.; Dmitri, A.; Rustam, K. On the effect of chemical composition on yield strength of TWIP steels. *Mater. Sci. Eng. A* **2017**, *687*, 82–84.
34. Kaye, G.W.C.; Laby, T.H. *Tables of Physical and Chemical Constants*, 14th ed.; Longman: London, UK, 1973.
35. Ding, H.; Li, H.Y.; Misra, R.D.K.; Wu, Z.Q.; Cai, M.H. Strengthening mechanisms in low density Fe-26Mn-xAl-1C steels. *Steel Res. Int.* **2018**, *89*, 1700381. [[CrossRef](#)]
36. Cao, J.; Yong, Q.; Liu, Q.; Sun, X. Precipitation of MC phase and precipitation strengthening in hot rolled Nb-Mo and Nb-Ti steels. *J. Mater. Sci.* **2007**, *42*, 10080–10084. [[CrossRef](#)]
37. Seok, M.-Y.; Choi, I.-C.; Moon, J.; Kim, S.; Ramamurty, U.; Jang, J.-I. Estimation of the Hall-Petch strengthening coefficient of steels through nanoindentation. *Scr. Mater.* **2014**, *87*, 49–52. [[CrossRef](#)]
38. Scott, C.; Remy, B.; Collet, J.-L.; Cael, A.; Bao, C.; Danoix, F.; Malard, B.; Curfs, C. Precipitation strengthening in high manganese austenitic TWIP steels. *Int. J. Mater. Res.* **2011**, *102*, 538–549. [[CrossRef](#)]
39. Wang, X.J.; Sun, X.J.; Song, C.; Chen, H.; Han, W.; Pan, F. Enhancement of yield strength by chromium/nitrogen alloying in high-manganese cryogenic steel. *Mater. Sci. Eng. A* **2017**, *698*, 110–116. [[CrossRef](#)]
40. Bouaziz, O.; Guelton, N. Modelling of TWIP effect on work-hardening. *Mater. Sci. Eng. A* **2001**, *319*, 246–249. [[CrossRef](#)]
41. Liang, Z.Y.; Li, Y.Z.; Huang, M.X. The respective hardening contributions of dislocations and twins to the flow stress of a twinning-induced plasticity steel. *Scr. Mater.* **2016**, *112*, 28–31. [[CrossRef](#)]
42. Chen, C.; Lv, B.; Feng, X.; Zhang, F.; Beladi, H. Strain hardening and nanocrystallization behaviors in Hadfield steel subjected to surface severe plastic deformation. *Mater. Sci. Eng. A* **2018**, *729*, 178–184. [[CrossRef](#)]
43. Wen, Y.; Xiao, H.; Peng, H.; Li, N.; Raabe, D. Relationship between damping capacity and variations of vacancies concentration and segregation of carbon atom in an Fe-Mn alloy. *Metall. Mater. Trans. A* **2015**, *46*, 4828–4833. [[CrossRef](#)]
44. Shen, T.; Schwarz, R.; Feng, S.; Swadener, J.; Huang, J.; Tang, M.; Zhang, J.; Vogel, S.; Zhao, Y. Effect of solute segregation on the strength of nanocrystalline alloys: Inverse Hall–Petch relation. *Acta Mater.* **2007**, *55*, 5007–5013. [[CrossRef](#)]
45. Vo, N.; Schäfer, J.; Averbach, R.; Albe, K.; Ashkenazy, Y.; Bellon, P. Reaching theoretical strengths in nanocrystalline Cu by grain boundary doping. *Scr. Mater.* **2011**, *65*, 660–663. [[CrossRef](#)]
46. Bobylev, S.; Enikeev, N.; Sheinerman, A.; Valiev, R. Strength enhancement induced by grain boundary solute segregations in ultrafine-grained alloys. *Int. J. Plast.* **2019**, *123*, 133–144. [[CrossRef](#)]

**Disclaimer/Publisher’s Note:** The statements, opinions and data contained in all publications are solely those of the individual author(s) and contributor(s) and not of MDPI and/or the editor(s). MDPI and/or the editor(s) disclaim responsibility for any injury to people or property resulting from any ideas, methods, instructions or products referred to in the content.